

# Thermal expansion and dehydroxylation of phengite micas

Mauro Gemmi · Marco Merlini ·  
Alessandro Pavese · Nadia Curetti

Received: 5 October 2007 / Accepted: 11 March 2008 / Published online: 2 April 2008  
© Springer-Verlag 2008

**Abstract** Phengite samples ( $2M_1$  and  $3T$  polytypes) and a synthetic end-member muscovite specimen were studied by in situ high-temperature synchrotron radiation X-ray diffraction. The measured volume thermal expansion of  $2M_1$  phengite ( $\langle\alpha_v\rangle \approx 36.6 \times 10^{-6} \text{ K}^{-1}$ ) was systematically greater than  $\langle\alpha_v\rangle$  of the  $3T$  polytype ( $\approx 33.3 \times 10^{-6} \text{ K}^{-1}$ ). A positive linear correlation between the average thermal expansion on (001) plane and the mean tetrahedral rotation angle at ambient condition is proposed on the ground of new measurements and literature data. Dehydroxylation processes were observed in  $2M_1$ , starting at 1,000 K in  $3T$  at 800 and 945 K in synthetic muscovite. Rietveld refinements allowed a determination of structural variations upon heating of phengite samples and their dehydroxylate phases. The phengite structure expands by regularizing the tetrahedral

sheet and by reducing the bond length differences between the outer and inner coordination shell of the interlayer site. The dehydroxylate phase derived from  $2M_1$  is characterized by fivefold polyhedra in the low temperature form as a consequence of two OH groups reacting to form  $\text{H}_2\text{O} + \text{O}$  (residual). The dehydroxylate exhibits an increase of the cation–cation distances along the M–O<sub>r</sub>–M bonds with respect to low-temperature phengite structures. For the  $3T$  phase, we were unable to achieve completion of dehydroxylation. The refined structural model of the dehydroxylate phase shows two hydroxyl sites, but at a short distance from one another. This result suggests that the dehydroxylation reaction did not proceed to completion.

**Keywords** Mica · Phengite · Thermal expansion · Dehydroxylation · Metamorphism

**Electronic supplementary material** The online version of this article (doi:10.1007/s00269-008-0230-x) contains supplementary material, which is available to authorized users.

M. Gemmi (✉) · A. Pavese  
Dipartimento di Scienze della Terra “A. Desio”,  
Università degli Studi di Milano,  
via Botticelli, 23, 20133 Milan, Italy  
e-mail: mauro.gemmi@unimi.it

M. Merlini  
ESRF, 6 rue Jules Horowitz, BP220,  
38043 Grenoble, France

A. Pavese  
National Research Council, IDPA, Section of Milan,  
Via Botticelli 23, 20133 Milan, Italy

N. Curetti  
Dipartimento Scienze Mineralogiche e Petrologiche,  
Università degli Studi di Torino,  
Via Valperga Caluso 35, 10025 Torino, Italy

## Introduction

Phengite micas [ideally  $\text{K}(\text{Mg}_{0.5}\text{Al}_{1.5})(\text{Al}_{0.5}\text{Si}_{3.5})\text{O}_{10}(\text{OH})_2$ ] are known to play a significant role in most petrogenetic reactions occurring in high-pressure (HP) metamorphic environments (see for instance: Ferrando et al. 2006; Keller et al. 2005; Massonne and Kopp 2005; Arkai 2002; Guidotti and Sassi 2002; Ferraris et al. 2000), and are extensively employed in dating HP rocks by determining the  $^{40}\text{Ar}/^{39}\text{Ar}$  ratio (see for example Di Vincenzo et al. 2006). Because of their stability in the HP regime, phengites are useful geothermobarometers both because they occur in common assemblages (Krogh-Ravna and Terry 2004; Massonne and Schreyer 1987, 1989) and because of the relative stabilities of the  $3T$  and  $2M_1$  polytypes (Sassi et al. 1994). High  $P/T$  ratio values supposedly promote the stability of  $3T$ , whereas low values seem to favor  $2M_1$ . This is presumably related to

cation ordering (Pavese et al. 1997, 1999a), and is governed by the equation of state (EoS), i.e., elastic and thermo-elastic properties and thermal expansion coefficients (Curetti et al. 2006; Pavese et al. 1999b). The EoS of  $2M_1$  and  $3T$  are very similar indicating that the relative polytypic stability is related to small differences in Gibbs energy. Thus, an accurate determination of the thermodynamic properties and the effect of composition may determine the role these micas have in metamorphic petrogenetic reactions.

Micas participate in reactions as  $H_2O$  carriers (Schmidt and Poli 1995) by releasing or storing  $H_2O$  in the form of hydroxyl (OH) groups. Therefore, in the thermal behavior of phengites is important: (1) the way in which phengites release  $H_2O$  and the dehydroxylation process, (2) the intermediate phases that may form, and (3) the relations between composition, polytype and transformation of kinetic mechanisms (Skjerlie and Douce 1999; Worden et al. 1992; Wirth 1985).

The present paper investigates the thermal behavior of phengites as a function of temperature ( $T$ ), by relating lattice parameters, structure and polytypic occurrence. In particular, we consider (1) thermal expansion and structural features at equilibrium at a given  $T$ , from ambient temperature to 780 K, and (2) dehydroxylation and related transformations occurring at higher temperature. This investigation was performed by in situ high-temperature X-ray powder diffraction, using the GILDA BM08 beamline at the European Synchrotron Radiation Facilities (ESRF) of Grenoble (France). The high  $2\theta$  resolution and excellent counting statistics achievable at a synchrotron experimental station allows (1) accurate cell parameters for

a precise determination of the thermal expansion curves, (2) a data set appropriate for the Rietveld analysis to obtain structural information related to  $T$  and (3) insight into the intermediate phases occurring during dehydroxylation.

Our work combines and complements previous in situ high-temperature studies on dioctahedral micas, among which we quote here, leaving out any claim of completeness, Mazzucato et al. (1999), Pavese et al. (2003), those reported in Table 3 by Zanazzi and Pavese (2002), Comodi et al. (2002), Mookherjee and Redfern (2002), Guggenheim et al. (1987) and Symmes (1986).

## Experimental

### Samples

We measured sundry natural phengite samples and one synthetic pure end-member muscovite specimen (Table 1). The muscovite end-member was synthesized from a fired gel as a starting material, in order to promote the synthesis at sub-solidus conditions. Gel has been prepared following the method of Hamilton and Henderson (1968) using tetraethylorthosilicate as a silica source, pure K- and Al- nitric solutions. An HP synthesis was performed in a single stage piston cylinder apparatus (calibrated against the albite = jadeite + quartz reaction at 600 and 800°C) adopting full salt assemblies and gold capsule. Run conditions were 1.1 GPa and 750°C for 281 h, at water-saturated conditions. The synthesis was performed at the Laboratory of Experimental Petrology, University of Milan, Italy.

**Table 1** List of the investigated mica samples

Sample	Polytype	Chemical composition	Provenance
MUS	$2M_1$	$KAl_2Si_3AlO_{10}(OH)_2$	Synthetic
AC	$2M_1$	$(K_{0.95}Na_{0.03})(Al_{1.57}Mg_{0.2}Fe_{0.25})(Si_{3.37}Al_{0.63})O_{10}(OH)_2$	Gneiss outcrop of Ahornach (Bolzano, Alto Adige, Italy)
FEM <sup>a</sup>	$2M_1$	$(K_{0.96})(Al_{1.49}Mg_{0.15}Fe^{2+}_{0.24}Fe^{3+}_{0.06}Ti_{0.03}Mn_{0.01})(Si_{3.45}Al_{0.55})O_{10}(OH)_2$	Metamorphic dike outcrop of Brossasco Isasca Unit, Western Alps (Italy)
BAM	$2M_1$	$(K_{0.83}Na_{0.07}Ba_{0.09})(Al_{1.52}Mg_{0.27}Fe_{0.26})(Si_{3.26}Al_{0.74})O_{10}(OH)_2$	Eclogite outcrop of Vara Inferiore (Voltri Group, Italy). Bocchio (2007)
SLT	$3T$	$(K_{0.94}Na_{0.01}Ba_{0.01})(Al_{1.35}Mg_{0.41}Fe^{2+}_{0.11}Fe^{3+}_{0.13})(Si_{3.46}Al_{0.54})O_{10}(OH)_2$	Metamorphic dike from Taohang region in the Dabie-Sulu ultra-high pressure terranes (Eastern China)
ECL	$3T$	$(K_{0.95}Na_{0.05})(Al_{1.48}Mg_{0.41}Fe^{2+}_{0.05}Fe^{3+}_{0.03}Ti_{0.02})(Si_{3.48}Al_{0.52})O_{10}(OH)_2$	Eclogite outcrop from Brossasco Isasca Unit, Western Alps (Italy)
FET <sup>a</sup>	$3T$	$(K_{0.96})(Al_{1.49}Mg_{0.15}Fe^{2+}_{0.24}Fe^{3+}_{0.06}Ti_{0.03}Mn_{0.01})(Si_{3.45}Al_{0.55})O_{10}(OH)_2$	Metamorphic dike outcrop of Brossasco Isasca Unit, Western Alps (Italy)
MGB	$3T$	$(K_{0.97}Na_{0.02})(Al_{1.44}Mg_{0.47}Fe^{2+}_{0.04}Fe^{3+}_{0.05}Ti_{0.02})(Si_{3.46}Al_{0.54})O_{10}(OH)_2$	Marble outcrop from Brossasco Isasca Unit, Western Alps (Italy)

<sup>a</sup> The sample FEM and FET are two polytypes coexisting in the same sample. Therefore, the chemical composition, reported as obtained at the microprobe, is an average composition

Each sample was initially examined by X-ray powder diffraction using a powder X<sup>pert</sup> PRO Philips diffractometer. The chemical compositions reported were determined as an average of at least 20 analysis points per specimen, measured by a WDS ARL-SEM-Q electron microprobe analyzer. Each point was measured with a beam current of 20 nA, a beam diameter of 20  $\mu\text{m}$ , a high tension of 15 kV and a counting time of 10 s on the peak and the background. The  $\text{Fe}^{3+}/\text{Fe}^{2+}$  ratio when reported was determined with Mössbauer spectroscopy.

#### Synchrotron radiation X-ray diffraction

The GILDA-BM08 beamline of ESRF (Grenoble) operates in Debye Scherrer geometry and is equipped with an imaging plate (IP) detector. The samples were encapsulated in quartz capillaries of 0.5 mm diameter and heated with a hot-gas blower from room temperature to 1,233 K for 180 min. The experiments were performed at an incident beam wavelength of 0.688767 Å, using an IP operated in translation mode as detector (Meneghini et al. 2001). The slit aperture, the translating system and the heating ramp were synchronized to obtain a time resolution of 3 min, corresponding to a diffraction pattern covering an interval of about 15 K in  $T$ . Sample-to-detector distance and detector-tilt angle were calibrated against standard LaB<sub>6</sub> (SRM 660a).

Diffraction images were integrated into  $2\theta$  patterns with the program “Scan\_Zero” (available at the beamline), which takes into account both the geometrical corrections to intensities and the zero angle correction.

Each pattern was analyzed by the Rietveld method implemented in the GSAS software package (Larson and Von Dreele 1988), refining the following overall parameters: scale factor; 25 coefficients of a Chebichev polynomial curve for the background; lattice parameters and zero shift; three parameters to model the full-width-at-half-maximum of the pseudo-Voigt profile function (one for the Gaussian and two for the Lorentian contribution, i.e., GW, LX and LY of GSAS coding); and a parameter to account for the anisotropic peak broadening owing to the lamellar shape of mica particles.

Data collection on MUS, AC, SLT and ECL resulted in sufficient quality to allow structure refinements; for each, the atomic coordinates and isotropic atomic displacement parameters were refined, constraining the atomic occupancies to the reported chemical compositions and the isotropic atomic displacement parameters of the oxygen atoms to be equal to each other. The  $2M_1$  samples were assumed in the space group  $C2/c$  using as a starting structure the one reported by Guggenheim et al. (1987). The  $3T$  sample structures were refined in space group  $P3_112$  employing as a starting structure that of Amisano-

**Table 2** Cell parameters and volume at room temperature

	$a(\text{Å})$	$b(\text{Å})$	$c(\text{Å})$	$\beta(^{\circ})$	$V(\text{Å}^3)$
<i>2M<sub>1</sub></i> samples					
MUS	5.1900(2)	9.0020(3)	20.1638(6)	95.781(2)	937.3(1)
AC	5.1987(2)	9.02101(4)	19.960(1)	95.750(3)	931.3(1)
BAM	5.2138(4)	9.0438(8)	19.946(2)	95.74(1)	935.9(2)
FEM	5.207(1)	9.041(2)	19.995(4)	95.62(2)	936.9(2)
<i>3T</i> samples					
SLT	5.2238(2)		29.754(2)		703.2(1)
ECL	5.2088(2)		29.745(1)		698.9(1)
FET	5.2191(2)		29.762(1)		702.1(1)
MGB	5.2290(1)		29.861(1)		707.0(1)

Canesi et al. (1994). The same space groups were maintained for the refinement of the related dehydroxylated structures. The standard figures of merit of the Rietveld refinement, i.e.,  $R_p$  and  $wR_p$ , vary between 1.5–1.0% and 2.0–1.5% for AC, 3.2–2.8% and 5.1–4.5% for MUS, 4.5–3.2% and 6.6–5.8% for SLT, 4.8–5.1% and 7.8–7.0% for ECL.

We use the following notation for the atomic positions (Guggenheim et al. 1987; Amisano-Canesi et al. 1994; Ferraris and Ivaldi 2002): K, interlayer site; M2, M3, cation sites in the octahedral sheet (O-sheet); T1, T2, cation sites in the tetrahedral sheet (T-sheet); O1, O2, O3, basal oxygens of the T-sheet; O4, O5, apical oxygens of the T-sheet; O6, OH-oxygen. The origin is placed at the virtually vacant M1-position, corresponding to a trans-configuration.

The unit cell parameters and volume of the samples at room temperature are given in Table 2.

**Table 3** Volume and edge thermal expansion coefficients and mean tetrahedral rotation angle at ambient condition of the investigated samples

	$\alpha_v$ $10^{-6}\text{K}^{-1}$	$\alpha_a$ $10^{-6}\text{K}^{-1}$	$\alpha_b$ $10^{-6}\text{K}^{-1}$	$\alpha_c$ $10^{-6}\text{K}^{-1}$	$\alpha_r$ ( $^{\circ}$ )	$\langle\alpha_v\rangle$
<i>2M<sub>1</sub></i> samples						
MUS	37.4(4)	10.0(1)	10.8(1)	17.0(1)	12.9(2)	36.6(4)
AC	36.7(4)	6.6(1)	9.4(1)	20.5(2)	8.3(2)	
BAM	36.2(2)	8.3(1)	9.0(1)	19.0(2)	–	
FEM	36.1(5)	9.4(3)	7.4(3)	19.5(2)	–	
<i>3T</i> samples						
SLT	31.3(2)	5.0(1)		21.3(2)	5.2(3)	33.3(4)
ECL	34.8(4)	7.2(1)		20.9(2)	6.8(3)	
FET	32.0(4)	5.3(2)		21.3(3)	–	
MGB	34.9(4)	6.9(2)		21.0(2)	–	

**Table 4** Volume and edge thermal expansion coefficients and mean tetrahedral rotation angle at ambient condition of micas, published in literature

Samples	$\alpha_V 10^{-6} \text{ K}^{-1}$	$\alpha_a 10^{-6} \text{ K}^{-1}$	$\alpha_b 10^{-6} \text{ K}^{-1}$	$\alpha_c 10^{-6} \text{ K}^{-1}$	$\alpha_r$ (°)
Muscovite-2M <sub>1</sub> (Catti et al. 1989)	42(8)	11.2(2)	11.8(3)	18.9(3)	11.8
Muscovite-2M <sub>1</sub> Panasqueira (Guggenheim et al. 1987)	35.4	9.3	9.8	15	11.8
Muscovite-2M <sub>1</sub> Keystone (Guggenheim et al. 1987)	34.7	9.9	11.1	10.5	11.3
Phengite-2M <sub>1</sub> (Mookherjee et al. 2001)	36	4.3	7.3	16.6	8.4
Phengite-2M <sub>1</sub> (Pavese et al. 1999a)	34.3(2)	8.9(2)	8.0(2)	16.6(1)	8.5
Paragonite-2M <sub>1</sub> (Comodi and Zanazzi 2000)	59(2)	15.1(8)	19.4(6)	21.5(7)	16.2
Phengite-3T (Pavese et al. 1997)	33.1(5)	5.7(1)		21.4(5)	5.5
Phengite-3T (Pavese et al. 2003)	34.0(5)	5.8(1)		22.3(5)	?
Fluorphlogopite-1M (Takeda and Morosin 1975)	39	9.8	9.3	17.3	6.4
Biotite-1M (Chon et al. 2003)	–	4.4	5.2	16.5	3.8
Phlogopite-1M (Russell and Guggenheim 1999)	–	14	13.4	18.1	11.3
Cs-Annite-1M (Comodi et al. 1999)	–	Negligible	Negligible	31.2	0.2

## Results

### Thermal expansion

Bulk and cell parameters thermal expansion coefficients are given in Table 3 and compared to literature values in Table 4. They have been calculated as:

$$\alpha_\ell(T) = 1/\ell(\partial\ell/\partial T)_P$$

( $\ell$ :  $a$ ,  $b$ ,  $c$ ,  $V$ ), using data collected over the  $T$ -interval 298–773 K, whereon micas preserve their OH content without dehydroxylation. Within experimental error, the measured thermal expansion is temperature independent, and thus  $\alpha(T) = \alpha_0$  suffices to fit the experimental data. The volume thermal expansion of 2M<sub>1</sub> phengites ( $\langle\alpha_V\rangle \approx 36.6 \times 10^{-6} \text{ K}^{-1}$ ) is systematically larger than phengite-3T ( $\langle\alpha_V\rangle \approx 33.3 \times 10^{-6} \text{ K}^{-1}$ ), but does not vary significantly within the same polytype. For 2M<sub>1</sub> polytypes, a remarkable scatter of  $\alpha_{a,b,c}$  is observed; this occurs in 3T also, but less pronounced.

### Dehydroxylation

MUS, AC, SLT and ECL samples gave high-quality diffraction patterns where it was possible to detect dehydroxylation (Fig. 1). Like thermal expansion, dehydroxylation is mainly affected by polytype structure, with 2M<sub>1</sub> and 3T showing different OH-release patterns. The chemical composition influences the dehydroxylation temperatures and the absolute cell parameter values. In Fig. 2 the variations of the cell edges of monoclinic MUS are shown (AC shows an analogous trend and it has not been reported for brevity; for comparison see Fig. 3 where normalized values are reported). Three regions are

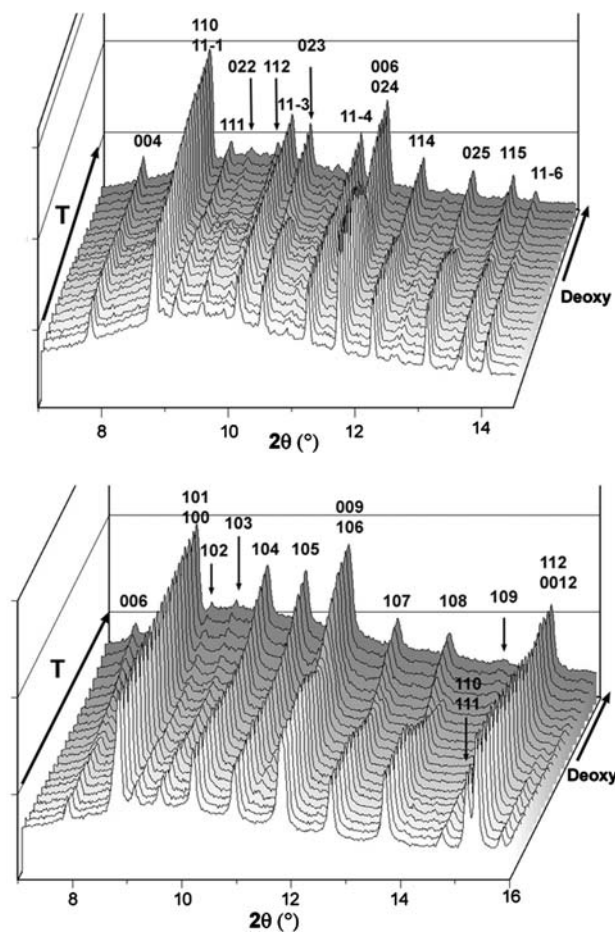


**Fig. 1** Three-dimensional plot of the low  $2\theta$  range of the high-temperature diffraction patterns of MUS (top) and SLT (bottom). The main diffraction peaks are indexed. The beginning of the dehydroxylation process is marked by a clear shift of some diffraction peaks (023 and 025 for MUS, 107 and 108 for SLT)

**Fig. 2** Cell parameters of synthetic muscovite as a function of temperature. Here and in following graphs, the *first point on the left* (plot at  $T = 250$  K to be distinguished) refers to the dehydroxylate phase at room temperature

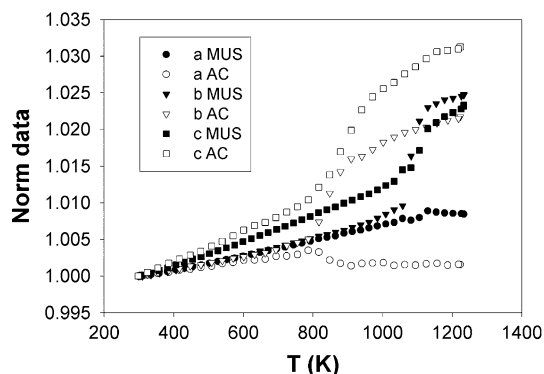
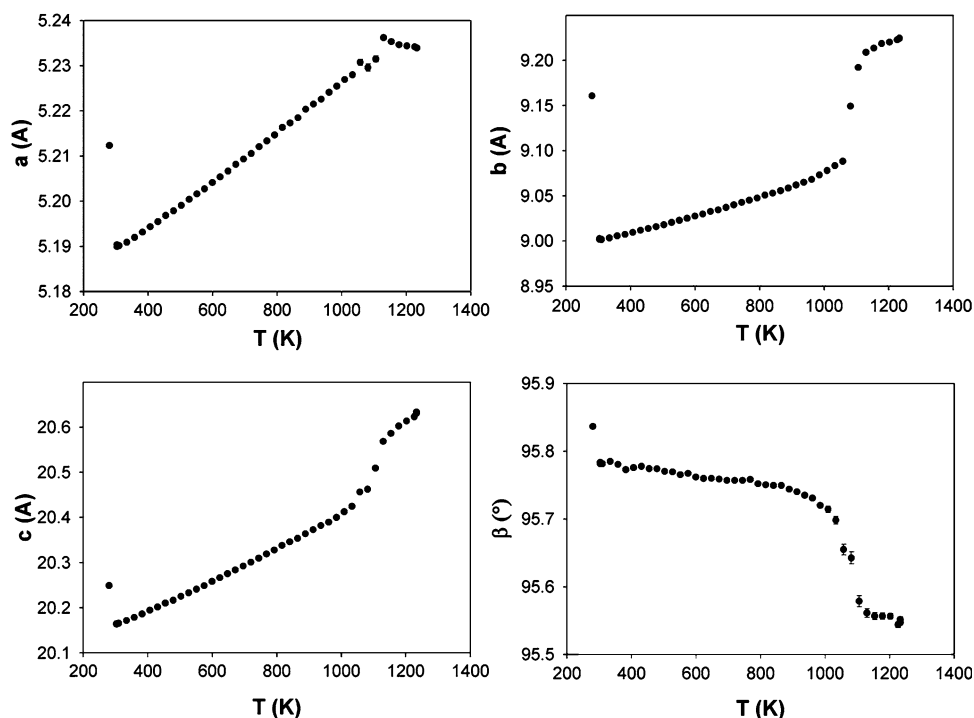


**Fig. 3** Cell parameters normalized to their room temperature values versus temperature, for MUS and AC samples

identified: a low temperature region where a sample has a mica structure; a region where dehydroxylation is in progress; a region at high temperature where the dehydroxylate phase exists. The dehydroxylation region is characterized by an irregular change of the  $a$  parameter, by a jump in value of both  $b$  and  $c$ , and by a decrease in the monoclinic angle  $\beta$ . The same behavior was observed for paragonite (Comodi and Zanazzi 2000) and by Guggenheim et al. (1987) for a muscovite specimen, although only limited data were given. We did not measure the thermal expansion of the dehydroxylated from ambient to the dehydroxylation temperature, but the limited data at  $T$  above dehydroxylation suggest  $\alpha_a \approx -3 \times 10^{-6} \text{ K}^{-1}$ ,  $\alpha_b \approx 11\text{--}9 \times 10^{-6} \text{ K}^{-1}$  and  $\alpha_c \approx 25\text{--}15 \times 10^{-6} \text{ K}^{-1}$  (for MUS and AC, respectively). These values are similar

to phengites (Table 3) except that  $\alpha_a$  is negative and near to 0. The most apparent difference between MUS and AC is the dehydroxylation temperature at  $\sim 1,000$  K and  $\sim 800$  K, respectively. The process ends in both samples at 1,150 K, as indicated by the more constant value in the  $\beta$  angle at higher  $T$ . Plotting the cell parameters normalized to their ambient values (Fig. 3) reveals that the relative variation of  $c$  during dehydroxylation is larger in AC than in MUS, whereas the opposite occurs for  $b$ .

The unit cell parameter variation during the dehydroxylation process for 3T is displayed in Fig. 4 for SLT and ECL samples. The transformation starts at  $\sim 945$  K, as indicated by the appearance of shoulders close to the main diffraction peaks (Fig. 5). The measured diffraction patterns may be fitted by two 3T structural models having different cell parameters. The phases co-exist for nearly 250 K above the dehydroxylation onset, the phase with the larger unit-cell volume becoming dominant while the other diminishes progressively upon  $T$ . The steep slope of  $a$  versus  $T$  (945–1,233 K range, Fig. 4) suggests that the dehydroxylation process is not complete at the highest temperature measured.

#### Structure as a function of temperature

The quality of the diffraction pattern for samples MUS, SLT and ECL allowed Rietveld refinements of the atomic positions for the high-temperature data of the heating ramp. The poor crystallinity of sample AC required that full image plate diffraction patterns with a longer exposure



**Fig. 4** Cell parameters of 3*T* SLT and ECL phengite samples as a function of temperature. Filled and empty circles represent the non-dehydroxylate and the dehydroxylate phase, respectively

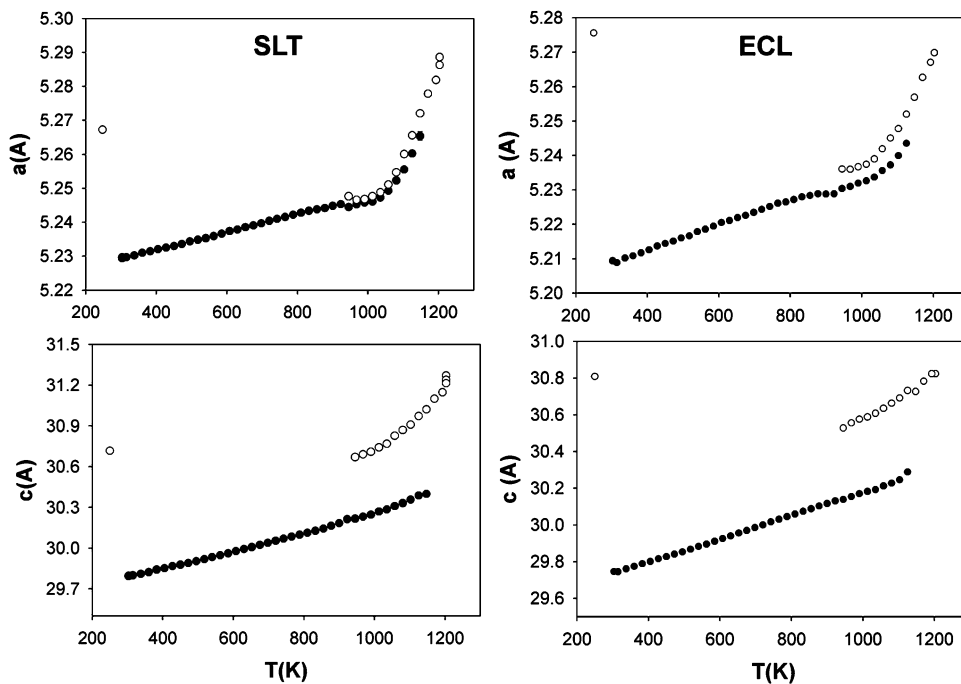
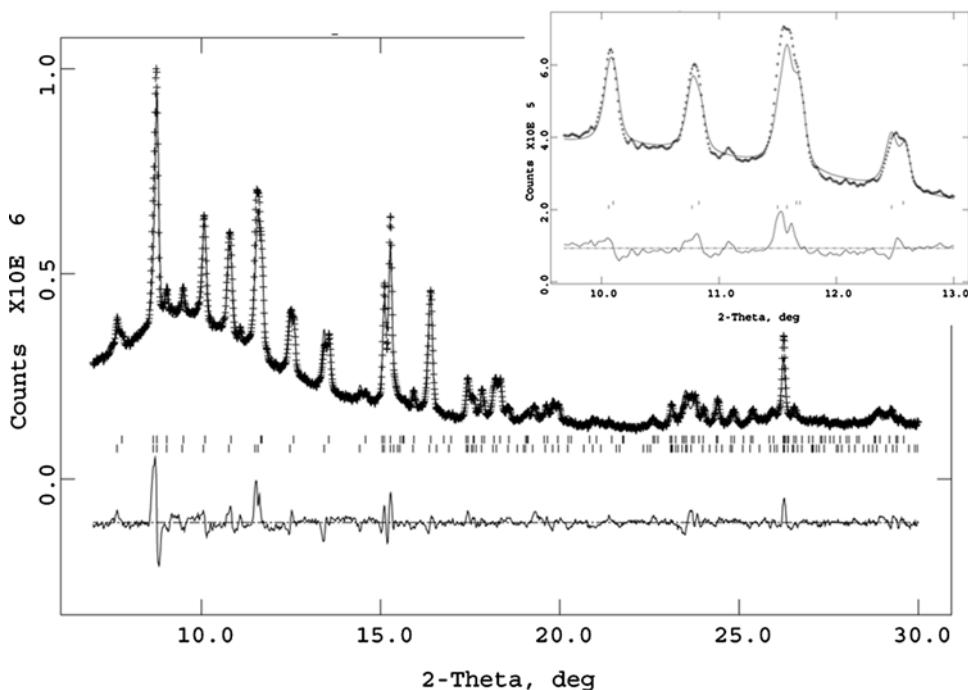


**Fig. 5** X-ray powder patterns of SLT sample at 1,100 K. The observed, calculated and residual patterns are reported. The fit has been performed considering two 3*T* phengite phases because of the presence of a clear peak splitting (see the box on the left)



time (15 min versus 2 min for patterns on the heating ramp) were recorded at 778, 923, 1,073 and 1,223 K, i.e., across and above the dehydroxylation *T*-region.

Because of the difficulties in determining structural details by Rietveld refinement in micas as a consequence of preferred orientation and possible stacking faults, we limit our discussion to average values and to bond distances exhibiting well-defined trends. Due to the high number of

refined structures, we do not report the atomic coordinates, which, however, are available on request from the authors.

Over the *T*-interval of phengite prior to dehydroxylation, only the interlayer region of the mica structure shows significant variations. The difference between the six inner and six outer shell K–O distances in MUS AC and ECL diminishes upon heating, leading to a more regular 12-fold K–O site as shown in Fig. 6. In SLT, the outer shell

**Fig. 6** Plots of the average K–O distance for the inner (black dots) and outer (white dots) shells

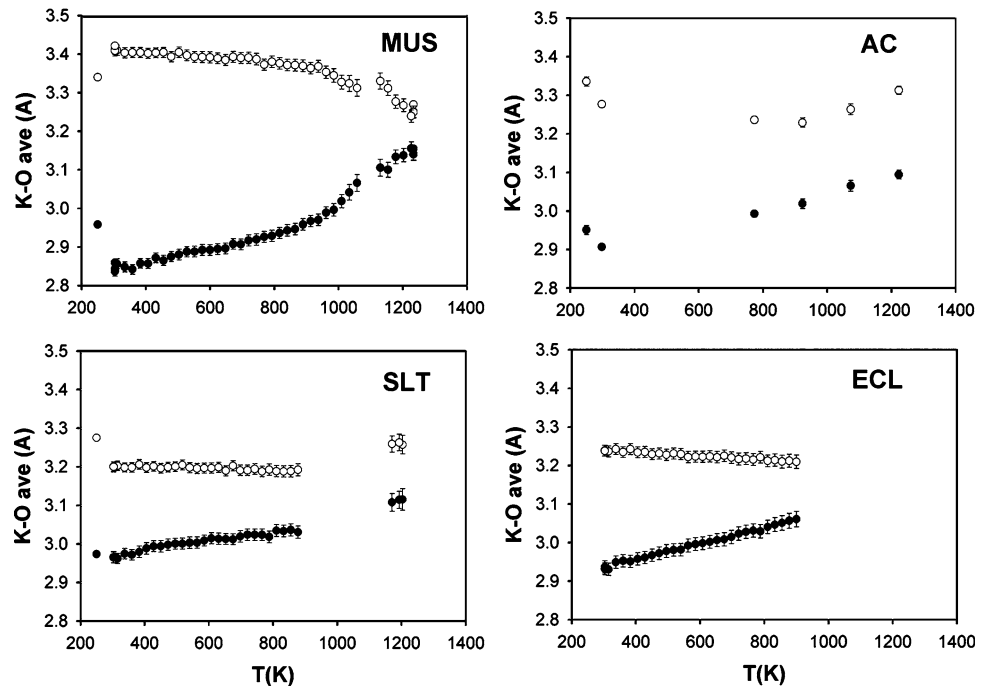
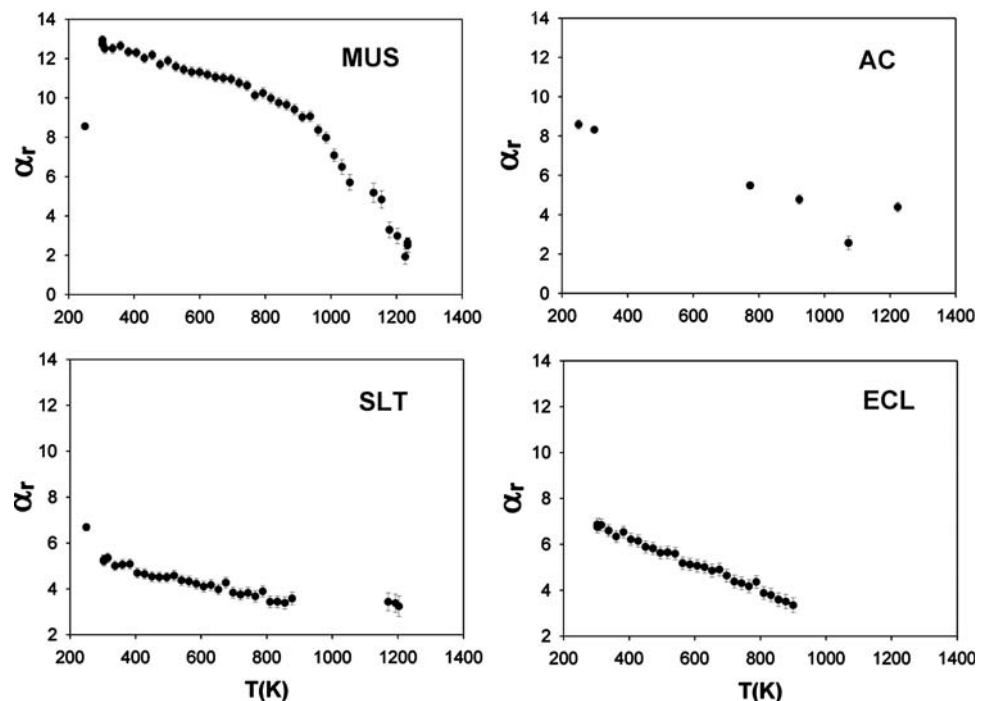


**Fig. 7** Mean tetrahedral rotation angle as a function of temperature



average K–O distance remains unchanged, and the inner shell shows an elongation of bond lengths. This change in the coordination shell of K is achieved through a regularization of the tetrahedral sheet. A plot of the mean tetrahedral rotation angle  $\alpha_r$  shows that in each investigated sample, it decreases upon heating (Fig. 7). Among the K–O distances, those involving O<sub>2</sub> oxygen systematically exhibit the highest sensitivity to heating (see Table 5). The O<sub>2</sub>

is the basal oxygen atom closest to the hydroxyl group. In muscovite the K–O<sub>2</sub> bond is weakened by the proton of the hydroxyl pointing in its direction (Rothbauer 1971; Guggenheim et al. 1987).

The octahedral and tetrahedral sheets show very small variations during thermal expansion. The average cation oxygen distances in both cases, either do not vary with temperature or changes do not exceed the estimated

**Table 5** Mean thermal expansion coefficients ( $10^{-5} \text{ K}^{-1}$ ) of K–O distances

$\alpha$ ( $10^{-5} \text{ K}^{-1}$ )	K–O1 short	K–O1 long	K–O2 short	K–O2 long	K–O3 short	K–O3 long
MUS	7.3	–2.2	7.6	–4.2	5.2	0.8
SLT	2.7	–0.5	9.9	–3.9	1.7	1.8
ECL	6.0	–2.6	10.1	–2.2	4.7	0.1

The coefficients are calculated as  $\beta/d_{300\text{K}}$ , where  $\beta$  is the slope of a linear fit of K–O as a function of  $T$  and  $d_{300\text{K}}$  is the bond distance at room temperature [see also Guggenheim et al. (1987)]

standard deviations (see Fig. 8). In  $3T$  samples, the two symmetry independent octahedra, related to the M2 and M3, exhibit different volumes, suggesting possible cation ordering consistent with Amisano-Canesi et al. (1994) and Pavese et al. (1997).

Cation order in the tetrahedral sheet may occur in  $2M_1$  MUS and AC samples, although the uncertainty in determining the T–O distances is too large to provide a definite answer (Fig. 9).

#### Structure of the dehydroxylate phase

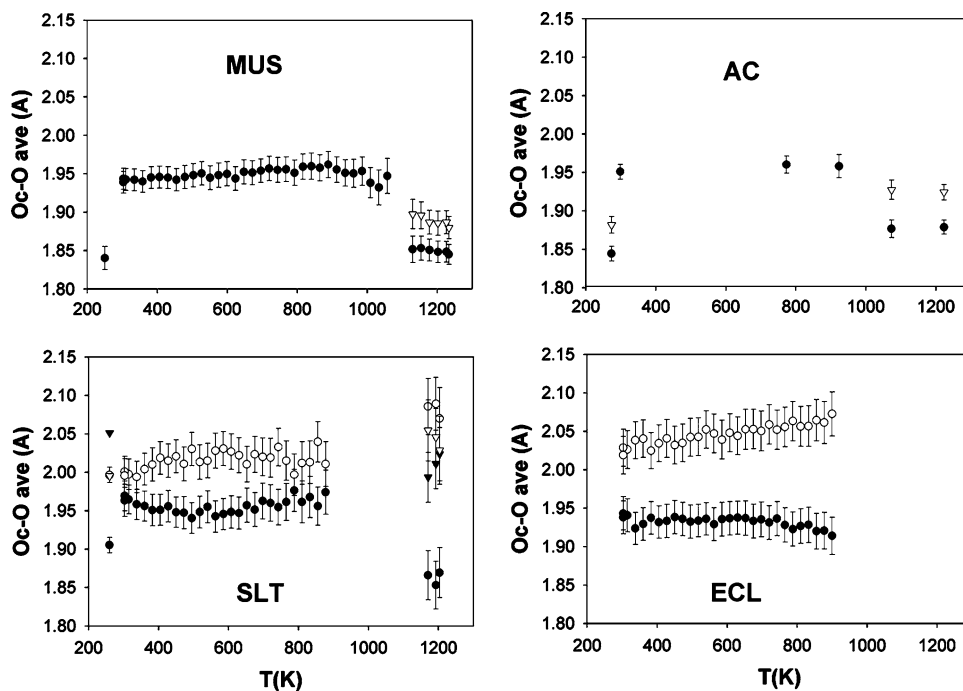
##### $2M_1$ phengite

In AC and MUS, dehydroxylation was completed in our experiments. The dehydroxylate structure is characterized by M sites with five nearest neighbors, as a result of replacing two hydroxyl groups with one “residual” oxygen (Or) in a special position (O6), i.e., the origin. Note that this five coordinated polyhedron was observed in natural

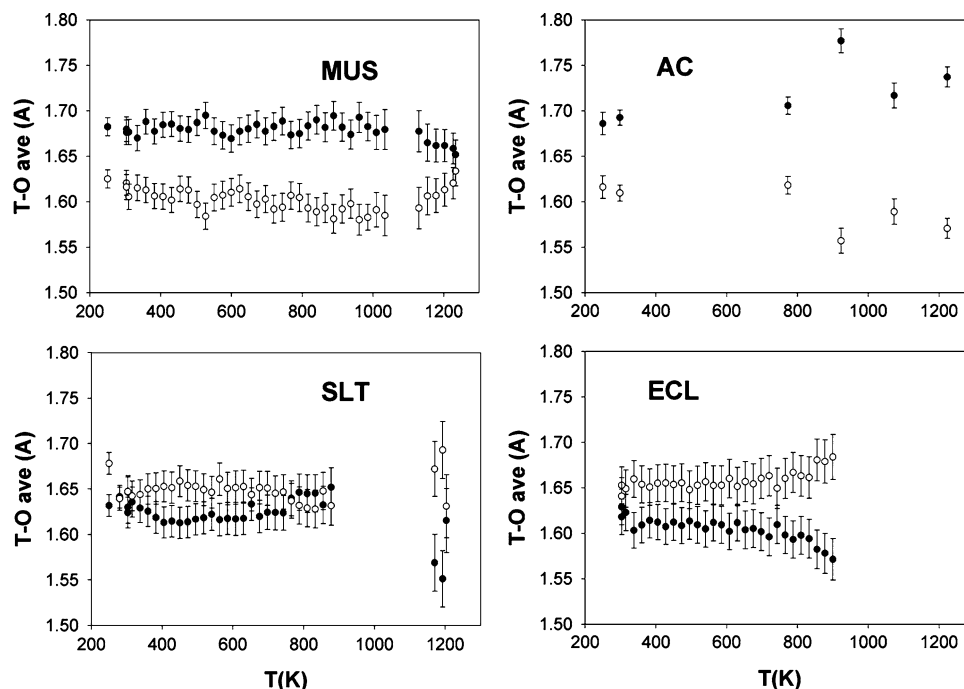
muscovite (Udagawa et al. 1974; Guggenheim et al. 1987), paragonite (Comodi and Zanazzi 2000) and pyrophyllite (Wardle and Brindley 1972). Such five coordinated polyhedra are distorted trigonal bi-pyramids, with the cation–Or distance being the shortest value. Every polyhedron shares two edges and a corner with three other polyhedra of the sheet, forming via Or mutually linked chains parallel to the [110] and [1–10] directions in alternate T–O–T modules (see Tables 6 and 7 for a list of unit cell parameters and the cation–oxygen distances and Fig. 10 for an illustration of the structure). The cation–cation distances along the chains (d2, d3) do not change significantly through dehydroxylation, whereas those involving polyhedra, which share corner (d1) and belong to adjacent chains, elongate (see Table 8). After dehydroxylation, the average cation–oxygen distance in the sheet containing five coordinated polyhedra exhibits shortening with respect to its value in the parent structure (see Fig. 8).

The tetrahedral sheet deforms in an analogous way. If, for convenience, we consider the tetrahedral sheet as formed by chains parallel to those defined for the sheet containing five coordinated polyhedra, the cation–cation distances normal to the chains increases after dehydroxylation (see Table 8). The tetrahedral sheet in the dehydroxylate is more regular than in the high-temperature mica phase, as shown by the  $\alpha_r$  angles and by the inner and outer shell K–O distances drawing closer to each other (see Figs. 6, and 7). In the dehydroxylate of MUS and AC cooled down to ambient condition, the tetrahedral sheet distorts back to  $\alpha \approx 8.5^\circ$  versus  $\alpha \approx 12.7^\circ$  and  $8.3^\circ$  in the MUS and AC phases, respectively.

**Fig. 8**  $\langle M2-O \rangle$  and  $\langle M3-O \rangle$  as a function of  $T$ . For the dehydroxylated phase: circles correspond to the distances between cation and oxygen atoms belonging to the same polyhedron; triangles represent the distances between cation and the apical oxygens, only, of the T-sheet





**Fig. 9**  $\langle T1-O \rangle$  and  $\langle T2-O \rangle$  as a function of temperature

### 3*T* phengite

Structural results are available only for SLT, because the Rietveld refinement on the ECL sample after dehydroxylation failed to provide realistic cation–oxygen distances.

The most satisfactory structure refinement of SLT after dehydroxylation was obtained by maintaining sixfold polyhedral coordination in the octahedral sheet, but allowing the two oxygen atoms of the hydroxyl groups to draw unlikely close to one another at 1.70 Å along the octahedral edge at high temperature, and at 1.68 Å after the quench (see Fig. 11). Such an inconsistency probably reflects a likely OH-disorder and an incomplete dehydroxylation reaction. In addition, there is an anomalously large rate of expansion of *a* above 1,100 K, which suggests an ongoing reaction. Thus, our structure model may represent an average of at least two co-existing OH configurations whose rearrangement is in progress.

Unfortunately, the experimental apparatus available does not allow temperatures greater than 1,233 K, and it is not possible to determine if the complete dehydroxylation of 3*T* phengites occurs before decomposition.

The symmetry-independent M2 and M3 sites in 3*T* give rise to two symmetry-independent sites in the dehydroxylate phase. The average cation–oxygen distances of these polyhedra significantly differ from each other. The Or atoms are closer to M2 than to M3 (see Table 7). If full dehydroxylation can be achieved, the two OH groups will merge into one position, as reasonably expected, and the dehydroxylate will have two different fivefold-coordination polyhedra. One, M2 will be similar to the fivefold polyhedron observed in 2*M*<sub>1</sub>, the other, M3, will have an average cation–oxygen bond length similar to that of the corresponding octahedron of the 3*T* phengite at ambient condition. An increase of the cation–oxygen distances along the M–Or–M bond occurs, as observed in 2*M*<sub>1</sub> (see Table 8 and Fig. 11).

**Table 6** Cell parameters and volume of the dehydroxylate phases

Sample	<i>a</i> (Å)	<i>b</i> (Å)	<i>c</i> (Å)	$\beta$ (°)	<i>V</i> (Å <sup>3</sup> )
MUS at 1,233 K	5.2339(3)	9.2242(6)	20.631(2)	95.551(4)	991.4(1)
MUS at 298 K	5.2123(2)	9.1611(4)	20.250(1)	95.836(3)	961.9(1)
AC at 1,223 K	5.2395(3)	9.2444(5)	20.695(2)	95.273(5)	998.1(1)
AC at 298 K	5.2204(4)	9.1916(6)	20.301(1)	95.539(5)	969.6(2)
SLT at 1,233 K	5.2692(3)	–	31.064(4)	–	746.9(2)
SLT at 298 K	5.2671(2)	–	30.718(2)	–	738.0(1)
ECL at 1,233 K	5.2743(6)	–	30.812(6)	–	742.3(2)

**Table 7** K–O, M–O and T–O distances of the dehydroxylate MUS, AC and SLT samples

	Inner shell			Outer shell				
	K–O1(Å)	K–O2(Å)	K–O3(Å)	K–O1(Å)	K–O2(Å)	K–O3(Å)		
Sample MUS								
MUS at rt	2.817(10)	2.833(14)	2.878(14)	3.324(11)	3.616(14)	3.286(14)		
MUS dehy at rt	2.924(15)	2.982(15)	2.968(14)	3.250(13)	3.520(12)	3.250(13)		
MUS dehy at 1,233 K	3.086(15)	3.145(16)	3.190(17)	3.172(13)	3.390(17)	3.186(17)		
Sample AC								
AC at rt	2.927(7)	2.852(8)	2.942(8)	3.282(7)	3.276(8)	3.273(9)		
AC dehy at rt	2.901(10)	3.012(11)	2.931(14)	3.292(9)	3.386(12)	3.330(14)		
AC dehy at 1,223 K	3.005(10)	3.150(11)	3.128(12)	3.299(8)	3.480(11)	3.161(11)		
Sample SLT								
SLT at rt	2.984(14)	3.013(12)	2.900(16)	3.065(11)	3.252(14)	3.281(13)		
SLT dehy at rt	3.014(15)	2.965(13)	2.941(14)	3.286(14)	3.470(15)	3.069(14)		
SLT dehy at 1,233 K	3.13(3)	3.07(3)	3.14(3)	3.187(19)	3.43(3)	3.15(3)		
Octahedral sheet								
	M2–O4(Å)	M2–O4(Å)	M2–O5(Å)	M2–O5(Å)	M2–O6(Å)	M2–O6(Å)		
Sample MUS								
MUS at rt	1.891(14)	1.882(11)	1.968(16)	1.997(16)	1.946(12)	1.949(14)		
MUS dehy at rt	1.882(13)	1.736(12)	1.800(15)	1.943(16)	1.699(7)	–		
MUS dehy at 1,233 K	1.963(14)	1.773(14)	1.776(15)	2.007(14)	1.706(7)	–		
Sample AC								
AC at rt	1.920(10)	1.937(7)	1.937(11)	1.885(10)	1.966(7)	2.061(10)		
AC dehy at rt	1.959(10)	1.783(10)	1.796(10)	1.988(11)	1.694(5)	–		
AC dehy at 1,223 K	2.096(10)	1.803(10)	1.727(10)	2.071(9)	1.697(5)	–		
	M2–O4(Å)	M2–O5(Å)	M2–O6(Å)	M3–O4(Å)	M3–O5(Å)	M3–O6(Å)		
Sample SLT								
SLT at rt	1.973(18)	2.02(3)	1.901(18)	1.93(2)	1.961(19)	2.092(2)		
SLT dehy at rt	2.212(16)	1.89(2)	1.613(18)	2.01(2)	1.98(2)	2.00(2)		
SLT dehy at 1,233 K	2.12(2)	1.93(4)	1.56(3)	2.04(5)	2.01(4)	2.15(3)		
Tetrahedral sheet								
	T1–O1(Å)	T1–O2(Å)	T1–O3(Å)	T1–O4(Å)	T2–O1(Å)	T2–O2(Å)	T2–O3(Å)	T2–O5(Å)
Sample MUS								
MUS at rt	1.703(17)	1.666(13)	1.619(12)	1.732(12)	1.592(16)	1.613(12)	1.648(12)	1.611(14)
MUS dehy at rt	1.60(2)	1.731(15)	1.640(13)	1.764(12)	1.627(18)	1.608(16)	1.586(16)	1.679(15)
MUS dehy at 1,233 K	1.54(2)	1.702(16)	1.649(14)	1.717(12)	1.61(2)	1.623(16)	1.580(15)	1.724(15)
Sample AC								
AC at rt	1.713(10)	1.696(8)	1.645(8)	1.716(7)	1.519(10)	1.712(7)	1.569(8)	1.640(7)
AC dehy at rt	1.725(16)	1.730(12)	1.604(11)	1.684(10)	1.526(15)	1.654(11)	1.644(13)	1.640(10)
AC dehy at 1,223 K	1.810(14)	1.812(11)	1.699(9)	1.627(9)	1.519(11)	1.592(10)	1.577(10)	1.595(11)
Sample SLT								
SLT at rt	1.633(16)	1.673(19)	1.617(13)	1.60(2)	1.682(15)	1.622(18)	1.646(16)	1.639(19)
SLT dehy at rt	1.74(3)	1.62(2)	1.696(14)	1.46(2)	1.58(2)	1.76(2)	1.689(19)	1.69(2)
SLT dehy at 1,233 K	1.61(4)	1.70(4)	1.66(3)	1.49(4)	1.64(3)	1.73(4)	1.55(3)	1.60(4)

We report data measured at the highest temperature and at room conditions after quenching. For the sake of comparison, the distances obtained before the heating ramp are listed too

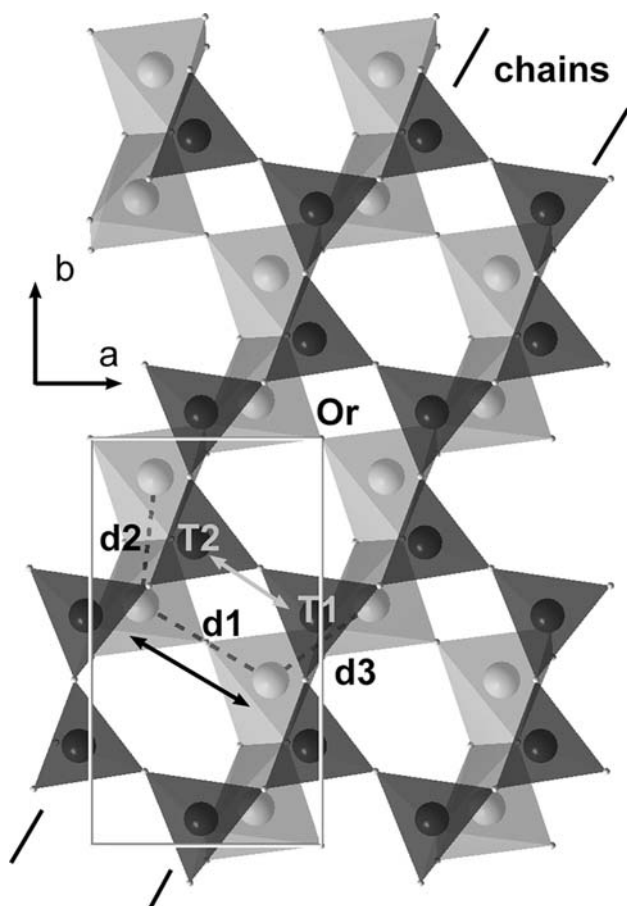


**Fig. 10** T–O–T module of quenched dehydroxylated  $2M_1$  structure (MUS) viewed along a direction close to the  $c$ -axis. The arrows indicate cation–cation distances that increase through the phase transition

**Discussion**

The investigated phengites show that  $2M_1$  samples exhibit larger  $\alpha_V$ 's than  $3T$ , independently of their chemical composition. This is in contrast with that reported in literature, especially for  $2M_1$ . Although the only data available for  $3T$  are in agreement with our results (Pavese et al. 1997, 2003), at least one of the two muscovites

investigated by Guggenheim et al. (1987) shows an  $\alpha_V$  that falls in the variation range of our  $3T$ , suggesting that polytypism is not the only factor governing volumetric thermal expansion. A careful investigation of the mechanism of distortion of the phengite structure with temperature can explain the main factor governing the thermal behavior of these minerals. Most of the thermal expansion of the phengites involves only modification in the K–O coordination shell that regularizes (Fig. 6) by means of two mechanisms: (1) dilation of the interlayer along  $c$ , and (2) regularization of the tetrahedral sheet through mutual rotation of the tetrahedral and consequent decrease of the mean tetrahedral rotation angle (Fig. 7). Mechanism (2) is responsible for the thermal expansion along the (001) plane and should be correlated with the distortion of the tetrahedral layer at ambient condition. To prove that, we plot the average thermal expansion coefficient of the (001) plane [ $(\alpha_a + \alpha_b)/2$  for  $2M_1$  and  $\alpha_a$  for  $3T$ ] versus the mean tetrahedral rotation angle ( $\alpha_r$ ) at ambient condition (Fig. 12) for all the data available on dioctahedral and trioctahedral micas. The linear correlation is evident; the more distorted the tetrahedral sheet, the more does the mica expand along  $a$  and  $b$ . This explains the great variability of the thermal expansion normal to  $c$ , and why a simple correlation between the thermal properties and the chemical composition of phengites cannot be found. The slope of the linear correlation seems to be steeper in the case of trioctahedral micas; however, more data are needed to confirm this trend.

Micas undergo partial to full dehydroxylation upon heating, following two possible reactions: (1) two hydroxyl groups belonging to an octahedron are replaced by one O atom and a molecule of  $H_2O$  is released (“pure” dehydroxylation); (2)  $Fe^{2+}$  cations in the octahedral sheet are oxidized to  $Fe^{3+}$  and one H atom is released (deprotonation). The effect of these two mechanisms on structural parameters is different: pure dehydroxylation increases the interlayer thickness and consequently the  $c$  parameter, whereas deprotonation via Fe-oxidation reduces the octahedral thickness and consequently the unit cell volume and

**Table 8** Cation–cation distances in the octahedral and tetrahedral sheets

	d1(Å)	d2(Å)	d3(Å)	T1–T2(Å)		
MUS	3.025(11)	3.039(11)	2.921(11)	2.918(11)	2.96(1)	3.11(1)
MUS deoxy at rt	3.398(11)	2.884(13)	2.852(11)	2.938(13)	2.952(11)	3.216(10)
MUS deoxy at 1,233 K	3.413(11)	2.959(14)	2.807(12)	2.901(16)	3.034(14)	3.217(14)
AC at rt	3.035(7)	2.997(7)	2.982(8)	2.966(8)	2.956(7)	3.094(7)
AC deoxy at rt	3.388(9)	2.913(10)	2.852(9)	2.959(12)	2.961(10)	3.208(9)
AC deoxy at 1,223 K	3.376(10)	2.904(10)	2.914(10)	2.998(11)	2.915(9)	3.272(9)
SLT at rt	3.030(19)	3.009(10)		2.96(2)	2.993(12)	3.103(15)
SLT deoxy at rt	3.18(3)	2.970(13)		3.08(3)	2.881(18)	3.167(2)
SLT deoxy at 1,233 K	3.29(4)	2.93(2)		2.98(5)	2.92(3)	3.24(3)

The labels correspond to the distances displayed in Figs. 10 and 11

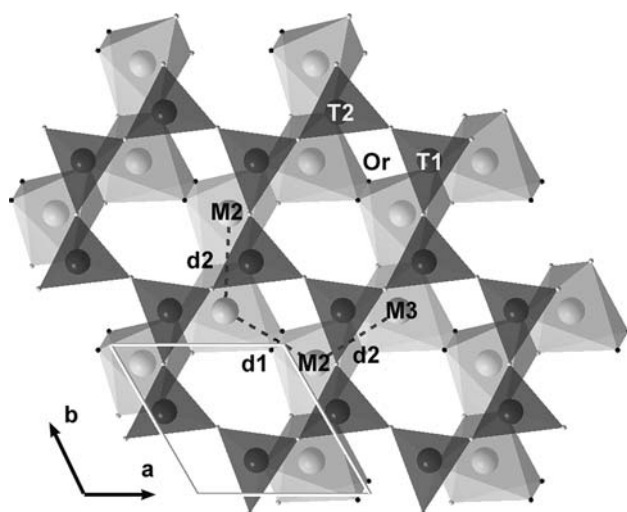


**Fig. 11** T–O–T module of quenched dehydroxylated 3T structure (SLT) projected along the  $c$ -axis. The arrows indicate cation–cation distances that increase through the phase transition

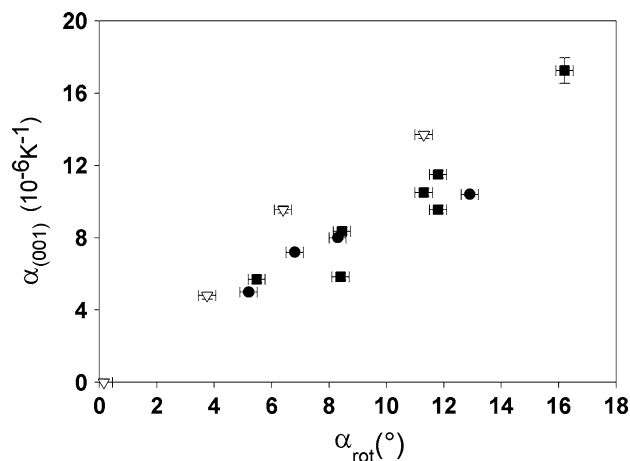


**Fig. 12** Plot of the average thermal expansion on the (001) plane  $\alpha_{(001)}$  [ $\alpha_{(001)} = (\alpha_a + \alpha_b)/2$  for  $2M_1$  and  $\alpha_{(001)} = \alpha_a$  for 3T] versus the mean tetrahedral rotation angle  $\alpha_r$  at ambient condition. Squares indicate  $2M_1$  3T phengites,  $2M_1$  muscovites and  $2M_1$  paragonite from literature. Triangles indicate 1M trioctahedral micas from literature. Circles indicate MUS, AC, SLT and ECL. Published data are summarized in Table 4

parameters (Russell and Guggenheim 1999; Chon et al. 2003). For the samples where we could follow the dehydroxylation process (MUS and AC for  $2M_1$ ; SLT and ECL for 3T), an expansion of the unit cell and a large increase of the  $c$  parameter were observed, independently of the Fe content. This suggests therefore that pure dehydroxylation is likely the primary mechanism and that Fe-oxidation is a minor process. This negligible influence of Fe-oxidation indicated that Mössbauer investigations to compare the  $Fe^{3+}/Fe^{2+}$  ratio before and after dehydroxylation were unnecessary. The difference in the observed dehydroxylation

temperatures between samples MUS, AC and the 3T, although measured with the same heating ramp, must be considered as a rough estimate. The observed temperatures are just an upper limit and more accurate kinetic studies are needed to precisely determine the correct transition temperature.

The structural rearrangement due to dehydroxylation may be depicted in terms of an increase in the cation–cation distance of the original octahedral sheet along the M–Or–M bonds. Such a configuration, which involves the whole T–O–T layer, is maintained by the quenched dehydroxylated phase and is responsible for the increase of  $a$  and  $b$  parameters with respect to those of the parent phase.

**Acknowledgments** We thank, Carlo Meneghini and all the staff of the GILDA beamline (BM08) at ESRF for technical assistance during synchrotron radiation experiments. The authors are indebted to Stefano Poli for providing the synthetic MUS sample, to Raffaele Sassi for providing several natural phengite specimens, and to Rosangela Bocchio for providing the BAM sample. The authors would also like to thank the two referees, S. Guggenheim and M. Mookherjee, for their valuable scientific comments and their kind revision of the English form.

## References

- Amisano-Canesi A, Chiari G, Ferraris G, Ivaldi G, Soboleva SV (1994) Muscovite- and phengite-3T crystal structure and conditions of formation. *Eur J Mineral* 6:489–496
- Arkai P (2002) Phyllosilicates in very low grade metamorphism: transformation to micas. In: Mottana A, Sassi FP, Thompson JB, Guggenheim S (eds) *Micas: crystal chemistry and metamorphic petrology*, vol 46. Reviews in Mineralogy and Geochemistry, Mineralogical Society of America, Chantilly, p 463
- Bocchio R (2007) Barium-rich phengite in eclogites from the Voltri Group (northwestern Italy). *Period Mineral* 76:155–167
- Catti M, Ferraris G, Ivaldi G (1989) Thermal strain analysis in the crystal structure of muscovite at 700°C. *Eur J Mineral* 1:625–632
- Chon C-H, Kim SA, Moon H-S (2003) Crystal structure of biotite at high temperatures and of heat-treated biotite using neutron powder diffraction. *Clays Clay Miner* 51:519–528
- Comodi P, Zanazzi PF (2000) Structural thermal behaviour of paragonite and its dehydroxylate: a high temperature single crystal study. *Phys Chem Miner* 27:377–385
- Comodi P, Zanazzi PF, Weiss Z, Rieder M, Drabek M (1999) “Cs-tetra-ferri-annite:” high-pressure and high-temperature behavior of a potential nuclear waste disposal phase. *Am Mineral* 84(2):325–332
- Comodi P, Gatta GD, Zanazzi PF, Levy D, Crichton W (2002) Thermal equations of state of dioctahedral micas on the join muscovite-paragonite. *Phys Chem Miner* 29:538–544
- Curetti N, Levy D, Pavese A, Ivaldi G (2006) Elastic properties and stability of coexisting 3T and  $2M_1$  phengite polytypes. *Phys Chem Miner* 32:670–678
- Di Vincenzo G, Tonarini S, Lombardo B, Castelli D, Ottolini L (2006) Comparison of Ar-40–Ar-39 and Rb–Sr data on phengites from the UHP Brossasco-Isasca unit (Dora Maira Massif, Italy): implications for dating white mica. *J Petrol* 47:1439–1465
- Ferrando S, Frezzotti ML, Dallai L, Compagnoni R (2006) Fluid-rock interaction in UHP phengite-kyanite-epidote eclogite from the Sulu Orogen, eastern China. In: Liou JG, Cloos M (eds) *Phase*

- relations, high-pressure terranes, P-T-ometry, and plate pushing; a tribute to W. G. Ernst International Book series, 9. Bellwether Publishing for the Geological Society of America, Columbia, p 250
- Ferraris G, Ivaldi G (2002) Structural features of micas. In: Mottana A, Sassi FP, Thompson JB, Guggenheim S (eds) Micas: crystal chemistry and metamorphic petrology, vol 46. Reviews in Mineralogy and Geochemistry, Mineralogical Society of America, Chantilly, p 499
- Ferraris C, Chopin C, Wessicken R (2000) Nano- to micro-scale decompression products in ultrahigh-pressure phengite: HRTEM and AEM study, and some petrological implications. *Am Mineral* 85(9):1195–1201
- Guggenheim S, Chang YH, Koster van Groos AF (1987) Muscovite dehydroxylation: high-temperature studies. *Am Mineral* 72:537–550
- Guidotti CV, Sassi FP (2002) Constraints on studies of metamorphic K-Na white micas. In: Mottana A, Sassi FP, Thompson JB, Guggenheim S (eds) Micas: crystal chemistry and metamorphic petrology, vol 46. Reviews in Mineralogy and Geochemistry, Mineralogical Society of America, Chantilly, p 413
- Hamilton DL, Henderson CMB (1968) The preparation of silicate compositions by a gelling method. *Mineral Mag* 36:832–838
- Keller LM, Abart R, Schmid SM, De Capitani C (2005) Phase relations and chemical composition of phengite and paragonite in pelitic schists during decompression; a case study from the Monte Rosa Nappe and Camughera-Moncucco Unit, Western Alps. *J Petrol* 46:2145–2166
- Krogh-Ravna EJ, Terry MP (2004) Geothermobarometry of UHP and HP eclogites and schists; an evaluation of equilibria among garnet-clinopyroxene-kyanite-phengite-coesite/quartz. *J Metamorph Geol* 22:579–592
- Larson AC, Von Dreele RB (1988) Laur 86-748, Los Alamos National Laboratory, Los Alamos, NM 87545
- Massonne HJ, Kopp J (2005) A low-variance mineral assemblage with talc and phengite in eclogite from the Saxonian Erzgebirge, Central Europe, and its P-T evolution. *J Petrol* 46:355–375
- Massonne HJ, Schreyer W (1987) Phengite geobarometry based on the limiting assemblage with K-feldspar, phlogopite and quartz. *Contrib Mineral Petrol* 96:212–224
- Massonne HJ, Schreyer W (1989) Stability field of the high pressure assemblage talc + phengite and two new phengite barometers. *Eur J Mineral* 1:391–410
- Mazzucato E, Artioli G, Gualtieri A (1999) High temperature dehydroxylation of muscovite-2M<sub>1</sub>: a kinetic study by in situ XRPD. *Phys Chem Miner* 26:375–381
- Meneghini C, Artioli G, Balerna A, Gualtieri AF, Norby P, Mobilio S (2001) Multipurpose imaging-plate camera for *in situ* powder XRD at the GILDA beamline. *J Synchrotron Radiat* 8:1162–1166
- Mookherjee M, Redfern SAT (2002) A high temperature Fourier transform infrared study of the interlayer and Si-O stretching region in phengite-2M<sub>1</sub>. *Clay Miner* 37:323–336
- Mookherjee M, Redfern SAT, Zhang M (2001) Thermal response of structure and hydroxyl ion of phengite-2M<sub>1</sub>. *Eur J Mineral* 13:545–555
- Pavese A, Ferraris G, Prencipe M, Ibberson R (1997) Cation site ordering in phengite 3T from the Dora-Maira massif (western Alps): a variable-temperature neutron powder diffraction study. *Eur J Mineral* 9:1183–1190
- Pavese A, Ferraris G, Pischedda V, Ibberson R (1999a) Tetrahedral order in phengite 2M<sub>1</sub> upon heating from powder neutron diffraction, and thermodynamic consequences. *Eur J Mineral* 11:309–320
- Pavese A, Ferraris G, Pischedda V, Mezouar M (1999b) Synchrotron powder diffraction study of phengite 3T from the Dora-Maira massif: P-V-T equation of state and petrological consequences. *Phys Chem Miner* 26:460–467
- Pavese A, Curetti N, Ferraris G, Ivaldi G, Russo U, Ibberson R (2003) Deprotonation and order-disorder reactions as a function of temperature in a phengite 3T (Cima Pal, western Alps) by neutron diffraction and Mössbauer spectroscopy. *Eur J Mineral* 15:357–363
- Rothbauer R (1971) Untersuchung eines 2M<sub>1</sub> Muskovits mit Neutronenstrahlen. *Neues Jahrb Mineral Monat* 143–154
- Russell RL, Guggenheim S (1999) Crystal structures of near-end-member phlogopite at high temperatures and heat-treated Fe-rich phlogopite: the influence of the O, OH, F site. *Can Mineral* 37:711–720
- Sassi FP, Guidotti CV, Rieder M, De Pieri R (1994) On the occurrence of metamorphic 2M<sub>1</sub> phengites: some thoughts on polytypism and crystallization condition of 3T phengites. *Eur J Mineral* 6:151–160
- Schmid M, Poli S (1995) H (sub 2) O transport and release in subduction zones; the role of lawsonite and phengite in metasomatizing the mantle. In: Schreyer W, Rummel F, Stoeckert B (eds) Abstract volume; International colloquium; High-pressure metamorphism in nature and experiment, vol 44. Bochumer Geologische und Geotechnische Arbeiten, Bochum, pp 209–210
- Skjerlie KP, Douce AEP (1999) High pressure (10–32 kbar) dehydration-melting of a zoisite phengite-bearing clogite from western Norway. *Eos Trans Am Geophys Union* 80(46 Suppl):1095
- Symmes GH (1986) The thermal expansion of natural muscovite, paragonite, margarite, pyrophyllite and two chlorites: the significance of high T/P volume studies on calculated phase equilibria. BA Thesis, Amherst College, Amherst
- Takeda H, Morosin B (1975) Comparison of observed and predicted structural parameters of mica at high temperatures. *Acta Crystallogr B* 31:2444–2452
- Udagawa S, Urabe K, Hasu H (1974) The crystal structure of muscovite dehydroxylate. *Japanese Assoc Mineral Petrol Econ Geol* 69:381–389
- Wardle R, Brindley GW (1972) The crystal structure of pyrophyllite, 1Tc, and of its dehydroxylate. *Am Mineral* 57:732–750
- Wirth R (1985) Dehydration and thermal alteration of white mica (phengite) in the contact aureole of the Traversella intrusion. *Neues Jahrb Mineral* 152:101–112
- Worden RH, Droop GTR, Champness PE (1992) The influence of crystallography and kinetics on phengite breakdown reactions in a low-pressure metamorphic aureole. *Contrib Mineral Petrol* 110:329–345
- Zanazzi PF, Pavese A (2002) Behavior of micas at high pressure and high temperature conditions. In: Mottana A, Sassi FP, Thompson JB, Guggenheim S (eds) Micas: crystal chemistry and metamorphic petrology, vol 46. Reviews in Mineralogy and Geochemistry, Mineralogical Society of America, Chantilly, p 499